ADVANCED QUANTUM TECHNOLOGIES
www.advquantumtech.com

Giant Anomalous Hall Conductivity in the Itinerant Ferromagnet $LaCrSb_3$ and the Effect of f-Electrons

Nitesh Kumar, Neetu Lamba, Jacob Gayles, Congcong Le, Praveen Vir, Satya N. Guin, Yan Sun, Claudia Felser, and Chandra Shekhar**

Itinerant ferromagnets constitute an important class of materials wherein spin polarization can affect the electric transport properties in nontrivial ways. One such phenomenon is anomalous Hall effect which depends on the details of the band structure such as the amount of band crossings in the valence band of the ferromagnet. Here, extraordinary anomalous Hall effect is found in an itinerant ferromagnetic metal $LaCrSb_3$. The rather 2D nature of the magnetic subunit imparts large anisotropic anomalous Hall conductivity of 1250 Ω^{-1} cm^{-1} at 2 K. The investigations suggest that a strong Berry curvature by abundant momentum-space crossings and narrow energy-gap openings are the primary sources of the anomalous Hall conductivity. An important observation is the existence of quasi-dispersionless bands in $LaCrSb_3$ which is now known to increase the anomalous Hall conductivity. After introducing f-electrons, anomalous Hall conductivity experiences more than twofold increase and reaches 2900 Ω^{-1} cm^{-1} in $NdCrSb_3$.

1. Introduction

Nontrivial band topology features a unique electronic structure that describes the origin of the quantum Hall effect, which exists with many variants. In the Hall effect, a mutually perpendicular magnetic field and electric current applied in materials causes a voltage perpendicular to them, i.e., the Hall voltage. Similarly, a comparatively large spontaneous Hall effect, termed the anomalous Hall effect (AHE), is known to exist in magnetic materials in which the Bloch wave function of electrons is asymmetric in momentum space. In this scenario, electrons acquire an additional group velocity in the presence of a driving perturbation, such as an external electric field. This anomalous velocity is perpendicular to the applied electric field, giving rise to an additional value to the Hall effect, i.e., AHE.[1] In addition, the group velocity is drastically enhanced by virtue of the Berry phase of nontrivial bands, which provides a strong fictitious field.

A nontrivial band topology arises when band inversion occurs, i.e., the conduction band is beneath the valence band with respect to their natural order in the vicinity of the Fermi level E_F (**Figure 1**a, left). Such inversion can be of several possible combinations among the s-, p-, d-, and f-bands. Figure 1a (right) shows a schematic of various types of band mixing; a resulting bandgap arises after considering spin–orbit coupling (SOC) regardless of their type. In such cases, the wave function of each band twists in momentum space inducing a nonzero Berry phase. A linear response of conductivity[2,3] from the Berry phase[4] for a 3D system is expressed in the Kubo formula

$$\sigma_{ij}^{A} = \frac{e^2}{\hbar} \sum_{n} \int \frac{d^3k}{(2\pi)^3} \Omega_{ij}^{n} f\left(\epsilon_k\right) \tag{1}$$

Ω_{ij}^{n} is the Berry curvature (BC), which crucially depends on the entanglement of bands. A small convergence of bands is caused by a large contribution from mixed occupied states, whereas its counterpart, i.e., unoccupied states, contributes negligibly. Therefore, AHE is rather large when the SOC-induced gap is small in the vicinity of E_F. The material selection and desired bandgap depend strongly upon the hybridization strength (by the lattice constant) and the magnitude of SOC (by the atomic charge). Interestingly, the dispersion of bands is a crucial factor and further depends on orbital hybridizations. For example, Figure 1b shows the calculated electronic band structure of $LaCrSb_3$, wherein several bands are relatively dispersionless, quite close to E_F along Y–Γ. Such bands are highly sensitive to perturbation and account for various intriguing phenomena such as nontrivial topology,[5–7] high-temperature fractional Hall effect,[6,8–11] unconventional superconductivity,[12,13] and unconventional magnetism.[7,14,15]

In our present selection of compound, i.e., $LaCrSb_3$ the quasi-dispersionless bands facilitate larger mixing of occupied and unoccupied bands close to E_F, that induces a large volume of BCs. Such BC associated with nontrivial bands as a source of AHE has recently been recognized in various compounds, for example,

Dr. N. Kumar, N. Lamba, Dr. J. Gayles, Dr. C. Le, Dr. P. Vir, Dr. S. N. Guin, Dr. Y. Sun, Prof. C. Felser, Dr. C. Shekhar
Max Planck Institute for Chemical Physics of Solids
Dresden 01187, Germany
E-mail: sun@cpfs.mpg.de; shekhar@cpfs.mpg.de

The ORCID identification number(s) for the author(s) of this article can be found under https://doi.org/10.1002/qute.202100023

DOI: 10.1002/qute.202100023

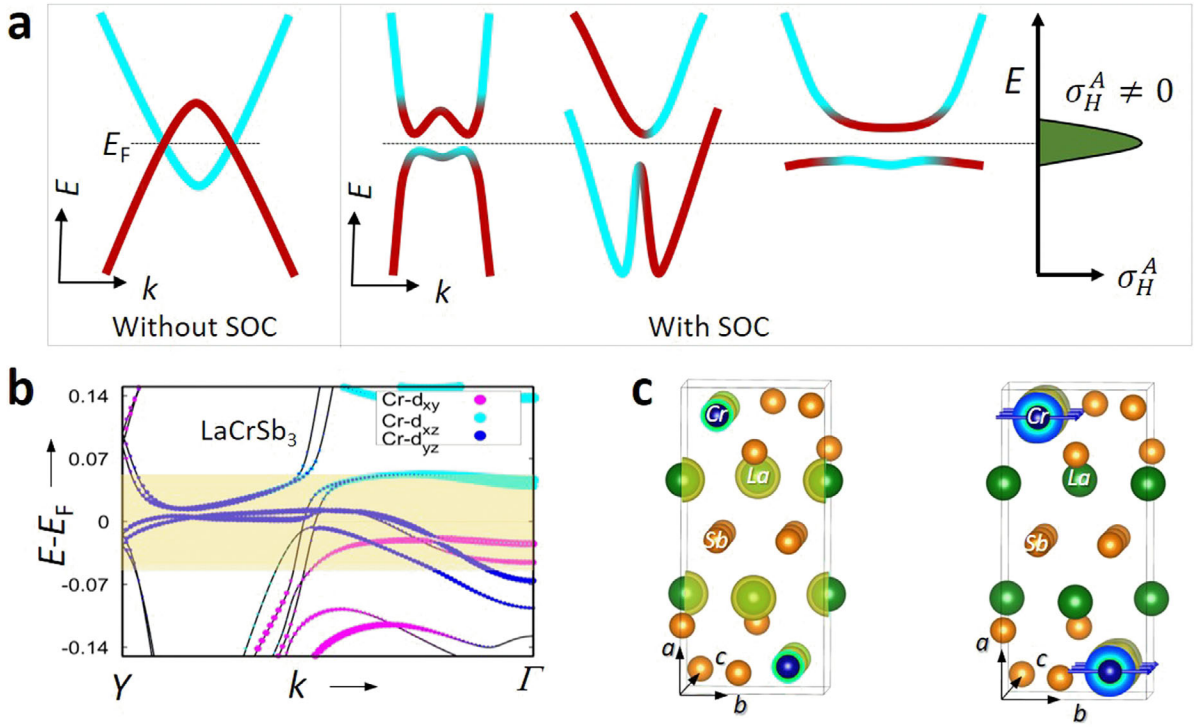

Figure 1. Nontrivial origins of anomalous Hall conductivity σ_H^A, band structure, Berry curvature (BC), and charge and spin densities. a) Schematic of different types of overlapping bands that result in zero (left) and nonzero (right) values of intrinsic σ_H^A, depending on spin orbit coupling (SOC). b) Orbital dependent electronic band structure of $LaCrSb_3$ along *Y*–Γ with SOC, depicting (shaded region) various quasi-dispersionless bands (very small change of energy with momentum) quite close to the Fermi energy, E_F. c) Charge density (left) and spin density (right) localization in $LaCrSb_3$.

chiral antiferromagnets Mn_3Sn and Mn_3Ge,[16,17] ferromagnetic massive Dirac metal Fe_3Sn_2,[18] and ferromagnetic nodal line compounds Co_2MnGa,[19,20] $Co_3Sn_2S_2$,[21] and Fe_3GeTe_2.[22]

2. Results

$LaCrSb_3$ possesses an orthorhombic centrosymmetric crystal structure and belongs to the *Pbcm* space group (No. 57). The lattice parameters *a*, *b*, and *c* for $LaCrSb_3$ are 13.18, 6.16, and 6.07 Å, respectively, and they decrease smoothly on replacing rare earth metals from La to Lu except for Yb.[23] In the crystal structure as shown in Figure S1a in the Supporting Information, the atoms are arranged in special manners: The Sb square nets form perpendicular to the [100]; the edge- and face-sharing of $CrSb_6$ octahedra arrange along the *b*- and *c*-axes, respectively. $CrSb_2$-magnetic layers in the *b*–*c* plane give rise to a 2D character to the crystal. The anion layers (Sb-square net and $CrSb_2$-layers) are separated by a cation La layer. These atomic arrangements are responsible for anisotropic electrical and magnetic properties.[24] From Figure 1c (left panel), electronic charge density is localized on Cr and La atoms. The $3d^3$ states of Cr^{3+} in each $CrSb_6$ octahedron experience the highest crystal field energy and they favorably split into e_g and t_{2g} energy levels, which are the main source of magnetism in this material (Figure 1c, right panel). These levels are split further among themselves. The orbitals $d_{x^2-y^2}$ and d_{z^2} split about 1.0 eV above and below the E_F, respectively, and give rise to 1 μ_B of magnetism. However, the t_{2g} states split and are localized in the order of meV around the E_F. This adds a small magnetic moment to the Cr atoms, due to the E_F lying in the middle of the band. Therefore, $LaCrSb_3$ is known to exhibit itinerant ferromagnetism.[25] The transition temperature T_C is 125 K and the spins are aligned in the *b*–*c* plane.[26] This means that the *b*- and *c*-axes are the easy axes, whereas the *a*-axis is the hard axis. Below 95 K, spins point 18° away from the *b*-axis in the *b*–*c* plane, reminiscent of an antiferromagnetic (AFM) component along the *c*-axis. Figure S2 in the Supporting Information shows the temperature-dependent resistivity behavior along different crystallographic axes; the resistivity rapidly decreases after T_C. Magnetization measurements are consistent with the *b*-axis being the easy axis; T_C also corresponds to that observed in the resistivity measurement (Figure S9, Supporting Information).

Electrical resistivity is directly related to the density of states of materials at E_F, whereas AHE is controlled by the BC concerning all the occupied states below E_F. We measured the Hall resistivity ρ_H and longitudinal resistivity ρ as a function of field *B* along all three crystallographic axes of $LaCrSb_3$ at varying temperatures, as shown in **Figure 2**a and Figure S3 in the Supporting Information, respectively. ρ_H shows anomalous behavior up to T_C (≈125 K) along the *b*- and *c*-axes (Figure S6, Supporting Information); their respective anomalous values at 2 K are 1.2 and 0.32 $\mu\Omega$ cm, whereas the *a*-axis data do not show any anomalous behavior (Figure 2a). The Hall conductivity is calculated according to the relation: $\sigma_{xy} = \frac{\rho_{yx}}{\rho_{yx}^2+\rho_{xx}^2}$. In Figure 2b, the corresponding anomalous Hall conductivity (AHC) are 1250 Ω^{-1} cm^{-1} for

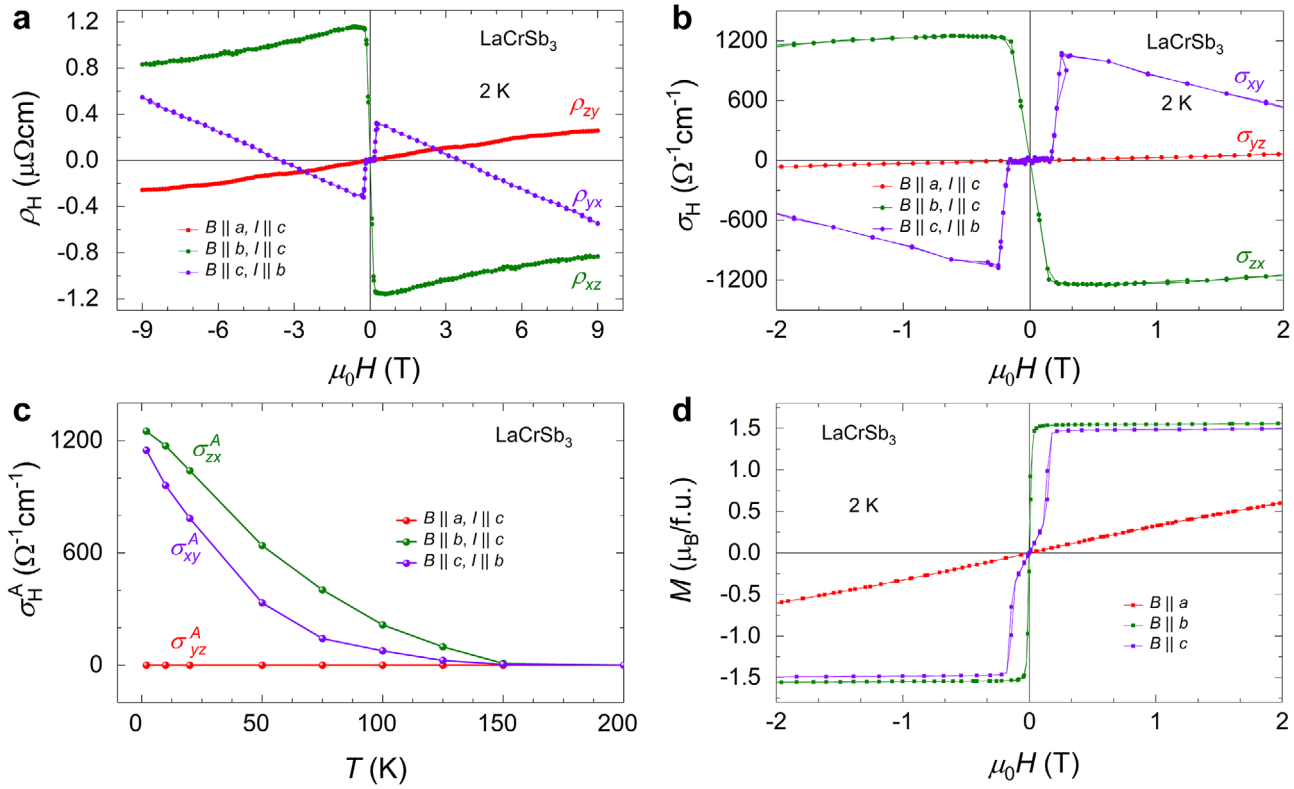

Figure 2. Hall resistivity ρ_H, Hall conductivity σ_H, and magnetization M of $LaCrSb_3$. a) Field-dependent behavior of ρ_H along the *a*-, *b*-, and *c*-axes at 2 K. The anomalous value of ρ_H, i.e., ρ_H^A, can be derived by extrapolating the high-field part of ρ_H to zero field. The field along the *a*-axis does not show anomalous behavior in ρ_H. b) The corresponding estimated value σ_H to measured data in (a). The anomalous value of σ_H, i.e., σ_H^A, can also be estimated similar to ρ_H^A. c) σ_H^A appears in both directions (*b*- and *c*-axes) up to 125 K, below the magnetic transition of $LaCrSb_3$. For example, σ_{xy} is calculated from the relation $\sigma_{xy} = \frac{\rho_{yx}}{\rho_{xx}^2+\rho_{xy}^2}$. d) Field-dependent magnetic measurements at 2 K along three crystallographic axes. The magnetic moments are easily aligned along the *b*- and *c*-axes and exhibit a similar saturation magnetization of 1.6 μ_B f.u.$^{-1}$, whereas the *a*-axis is a hard axis.

the *b*-axis and 1150 Ω^{-1} cm^{-1} for the *c*-axis at 2 K; which gradually decrease to zero as the temperature approaches T_c (Figure 2c). It should be noted that the Hall conductivity remains zero up to 0.17 T along *c*-axis after which it suddenly rises to attain the saturation. This behavior is consistent with the small AFM interaction along *c*-axis owing to the fact that the anomalous velocity over all the occupied states in an AFM is zero. It is clear that the measured AHE is strongly anisotropic and appears only when B applies in the *b*–*c* plane. Magnetic field-dependent magnetization measurements for $LaCrSb_3$ at 2 K along different crystallographic axes are shown in Figure 2d. The magnetic moments are easily aligned along the *b*- and *c*-axes, whereas *a*-axis is the hard axis, evidencing an anisotropic magnetic behavior. As compared to *b*-axis, magnetization along *c*-axis starts to increase slowly at small field, then suddenly jumps to saturation, accounting for the 18° spin canting toward the *c*-axis in the *b*–*c* plane. The saturation magnetization reaches 1.6 μ_B f.u.$^{-1}$ for $LaCrSb_3$, which is the same as previously reported.[25,26]

To gain an insight into the giant observed AHC, we used constrained-moment ab initio calculations with the local spin density approximation exchange-correlation potential to simulate the band structure of $LaCrSb_3$ with the experimental lattice parameters and magnetic moments with spins pointing along *b*-axis. We calculated the momentum space BC of the electronic structure, revealing a large volume, which is centered on the Γ point (**Figure 3**a). This originates further due to the inversion between Cr-d and Sb-p orbitals, forming rather dispersionless bands around this region. We found two interesting features: i) Nontrivial bands in the plane k_y–k_z that produce large nonzero BC.[10,11] This large volume of BC is different from normal magnetic metals, which show delta-like "hot" spots in the Brillouin zone (BZ), for example, *bcc* Fe.[2] Such a unique and large volume of BC distribution provides a giant AHC. ii) Trivial bands along k_x due to the weak coupling between Cr-Sb layers and La layers, producing the large longitudinal resistivity and negligible anomalous Hall effect as we have observed. Figure 3b–d shows the electronic band structures for $LaCrSb_3$ along the high symmetric points (shown by dashed green, black and pink lines), depicting many nontrivial nearly dispersionless bands in the vicinity of E_F. From their atomic orbital contributions as given in Figure S14 in the Supporting Information, these bands are mainly Cr-d dominated, which play a crucial role for the electric and magnetic properties. These nontrivial bands are localized around the center of the BZ along k_x. A recent study[27] on the effect of reducing band width in the enhancement of AHC is consistent with our observation of large AHC in quasi-dispersionless bands in $LaCrSb_3$ (see Figure S15, Supporting Information, for a tight binding method based toy model).

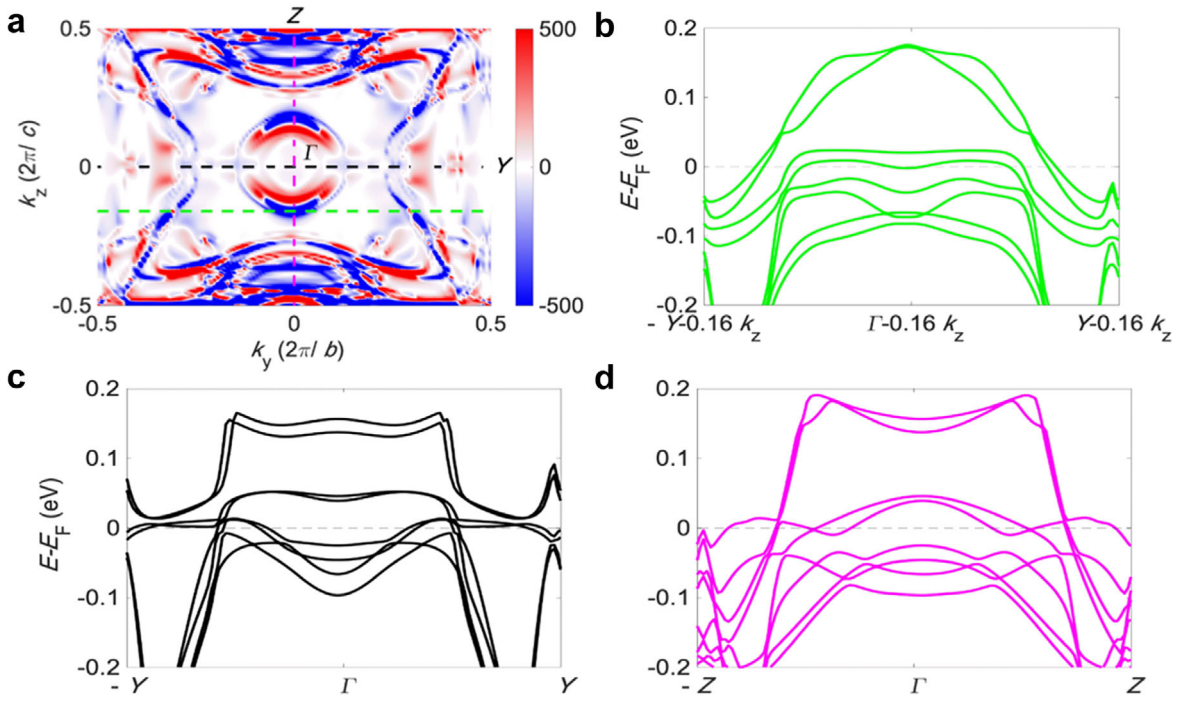

Figure 3. Berry curvature (BC) and corresponding bands of $LaCrSb_3$. a) Showing the large value of BC distribution of k_y–k_z plane (red as positive BC and blue as negative), in which plane the giant anomalous Hall conductivity is observed. b–d) The band energy dispersion corresponding the color dashed lines in (a) along b) Z–S (a path shifted $-0.16k_z$ from Γ–Y), c) Γ–Y, and d) Γ–Z high symmetry points of Brillouin zone, indicating the large value of BC is exhibited by the nontrivial less-dispersive bands.

2.1. Effect of f-Electron

After measuring the remarkable values of AHC in the parent compound $LaCrSb_3$, it is highly desirable to obtain understanding about the AHE behavior by measuring other compounds from $RCrSb_3$ series, where R is a rare earth element. Therefore, we extended our study to $CeCrSb_3$ and $NdCrSb_3$ possessing f-electrons and measured the field-dependent ρ_H and ρ values (Figures S4–S7, Supporting Information) at various temperatures. For $CeCrSb_3$, the measured anomalous values of ρ_H along b- and c-axes at 2 K are 4.3 and 5.2 μΩ cm, respectively (see Figure S6, Supporting Information). The resulting values of σ_H are plotted in **Figure 4** at various temperatures, which shows that the anomalous behavior of σ_H is quite similar to that of $LaCrSb_3$. The AHC of $CeCrSb_3$ at 2 K is 1550 Ω^{-1} cm^{-1} along both the b- and c-axes (Figure 4a) and the AHC of $NdCrSb_3$ at the same temperature is 2900 Ω^{-1} cm^{-1} for the b-axis (Figure 4b) and 900 Ω^{-1} cm^{-1} for the c-axis. As expected, these values decrease as temperature reaches at T_C (Figure 4c). Even though f-electrons introduce finite spontaneous magnetization along a-axis in $CeCrSb_3$ and $NdCrSb_3$, AHE is negligible for both compounds over the entire temperature range, as observed with $LaCrSb_3$. This demonstrates that Cr−d electrons are largely responsible for the AHE in this series of compounds. Moreover, there is no one-to-one correspondence between observed AHC and magnetic moment along various axes. This can be seen from the column plot in Figure 4d, signifying the role of electronic structure for AHC. For example, even though the magnetization of $NdCrSb_3$ is the highest along a-axis at 2 K but produces negligible AHC. The similar effect is also observed for $CeCrSb_3$. Among the series of compounds, $NdCrSb_3$ shows giant AHC, which is the highest ever measured in any material to the best of our knowledge. $NdCrSb_3$ has a larger moment as compared to $LaCrSb_3$ and $CeCrSb_3$, and that moment is weakly coupled to the Cr d-states. This is evident from a metamagnetic transition in magnetization and AHE data of $NdCrSb_3$ along b-axis. However, above the ordering temperature of Nd spins (12 K), the effect is lost and the behavior and value of AHC closely follow that of $LaCrSb_3$. Larger magnetic moment in $NdCrSb_3$ compared to $LaCrSb_3$ and $CeCrSb_3$ at low temperature could be one of the reasons for the existence of giant AHC. The observation that the AHC in $NdCrSb_3$ decreases sharply and closely follows that of $LaCrSb_3$ after Nd-spin ordering temperature, indicates that Cr-d electrons dominated in the larger part of the temperature range studied. Owing to the correlation effect for added f-electrons in $CeCrSb_3$ and $NdCrSb_3$, it is not straightforward to estimate AHC from first principles calculations. It should be noted that the sign of anomalous Hall resistivity differs for various axes in all three compounds despite maintaining the same measurement geometry. Hence, this sign is dictated by the sign of Berry curvature for a particular direction of applied magnetic field. For a broad comparison, the observed values of AHC of some notable compounds are shown in Figure S13 in the Supporting Information.

The anomalous behaviors in $RCrSb_3$ not only appear in electrical transport but are also found in thermal transport, i.e., the Nernst thermopower S. Figure S8 in the Supporting Information shows the field-dependent measured S_{xz} of $CeCrSb_3$ at different temperatures, affirming an anomalous behavior. The anomalous

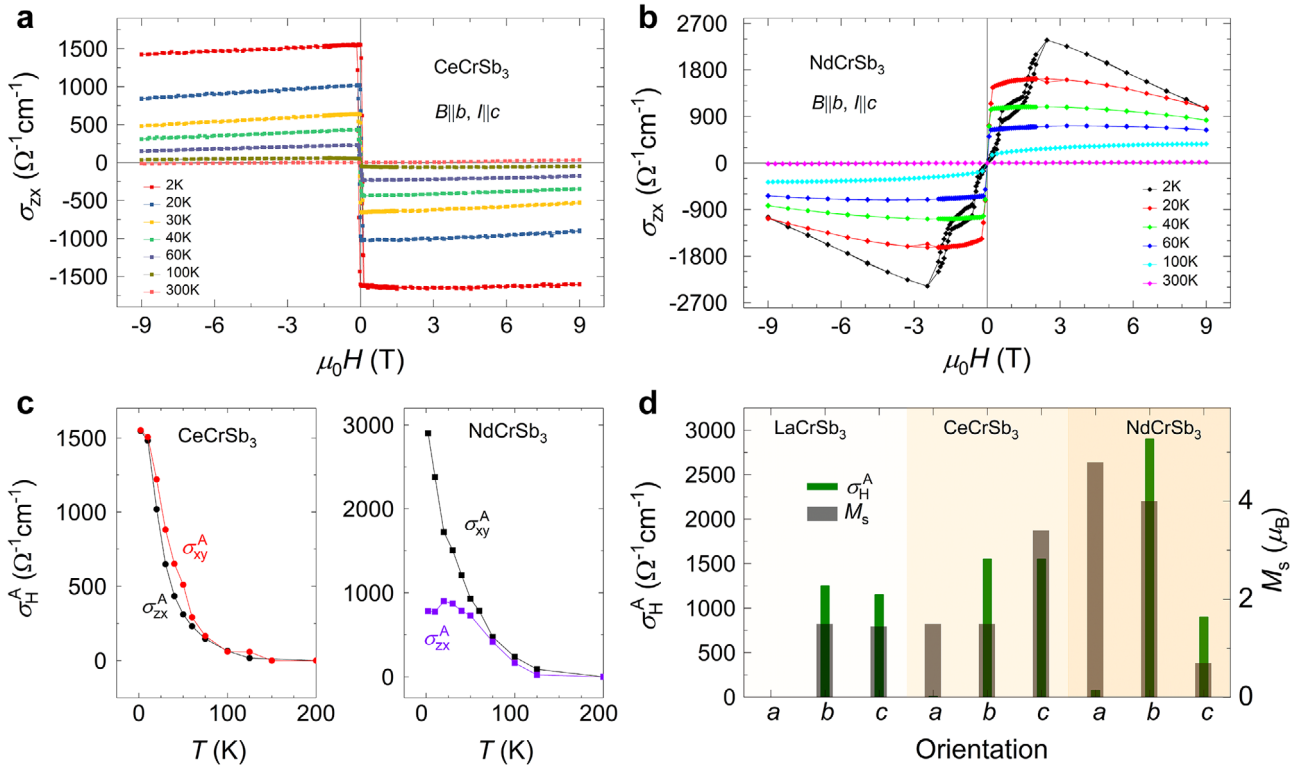

Figure 4. Hall conductivity σ_{zx}, anomalous Hall conductivity σ^{A}_{zx} of $CeCrSb_3$ and $NdCrSb_3$, and their σ^{A}_{H} value with saturation magnetization M_s. a) σ_H along $B \parallel b$, $I \parallel c$ for $CeCrSb_3$. b) σ_H along $B \parallel b$, $I \parallel c$ for $NdCrSb_3$. These measurements clearly show that the anomalous value of σ_H smoothly changes across the transition temperature of rare-earth metals, reflecting the negligible effect of their spins. c) Temperature evolution of σ^{A}_{H} of $CeCrSb_3$ (left panel) and $NdCrSb_3$ (right panel) along the *b*- and *c*-axes up to 200 K. The nonzero values of σ^{A}_{H} appear only below their magnetic transitions. d) Column plot of measured σ^{A}_{H} and M_s at 2 K with different orientations for $LaCrSb_3$, $CeCrSb_3$, and $NdCrSb_3$. Among them, $NdCrSb_3$ shows the largest value of σ^{A}_{H}.

Table 1. Anomalous values of studied compounds at 2 K. Anomalous Hall resistivity (AHR), anomalous Hall conductivity (AHC), resistivity (ρ), charge carrier density (n), anomalous Hall angle (AHA), ferromagnetic transition temperature (T_c).

Compound	$B \parallel$	T_c [K]	ρ [10^{-5} Ωcm]	n [10^{22} cm^{-3}]	AHR [μΩcm]	AHC [Ω^{-1} cm^{-1}]	AHA [%]
$LaCrSb_3$	*a*-axis	125	30.27	2.12	0	0	0
	b-axis		1.75		1.21	1250	4
	c-axis		3.04		0.32	1150	1.8
$CeCrSb_3$	*a*-axis	125		0.92	0.19	10	0.18
	b-axis		5.33		4.3	1550	8.1
	c-axis		5.19		5.2	1550	10.0
$NdCrSb_3$	*a*-axis	116		1.62	0.8	75	0.77
	b-axis		3.26		2.5	2900	7.7
	c-axis		4.98		1.2	900	2.5

value of S_{xz} is found to be 2.5 μV K^{-1} at 21 K, which associates these compounds with the nontrivial materials, exhibiting high anomalous Nernst effect.[20,28]

Another important parameter, anomalous Hall angle (AHA), defines as how much longitudinal current coverts into the transverse direction. The estimated AHA is 4–10% for the present series of compounds (see **Table 1**). It is notable that despite a large carrier concentration ≈ 10^{22} cm^{-3}, the value of AHA compares to materials like Weyl semimetal $Co_3Sn_2S_2$ where the carrier concentration is at least two orders of magnitude smaller.[21,29]

3. Discussion

$RCrSb_3$ is a promising series of quasi-2D compounds that exhibit high anisotropic AHC. The measured AHC is the sum of

all the contributions from the entire BZ and that can have both intrinsic and extrinsic origins. From the framework of unified models that are valid for the varieties of compounds having conductivity beyond the range of $10^4 < \sigma < 10^6\ \Omega^{-1}\ cm^{-1}$, extrinsic origins dominate.[30,31] The conductivity of the RCrSb$_3$ series of compounds ranges from 0.7×10^4 to $5.9 \times 10^5\ \Omega^{-1}\ cm^{-1}$, which lie within the moderate range of conductivity. The temperature-dependent data of σ_H^A versus σ are neither constant nor linear, excluding the single contribution from the Berry phase or skew scattering (Figure S12, Supporting Information). However, from the power law behavior $\sigma_H^A \propto \sigma^n$, n is found to be 1.7 for LaCrSb$_3$ and CeCrSb$_3$ (Figure S12, Supporting Information). For cases where a mixed contribution of Berry phase and side-jump dominates, n is predicted to be 1.6.[32] Surprisingly, our estimation of $n = 3$ for NdCrSb$_3$ goes beyond this power law and calls for more accurate scaling law. Due to nonlinear behavior of σ_H^A versus σ^2, it is hard to estimate the accurate value of AHC from Berry phase by a linear intercept method. To naively check, a rough linear intercept of σ_H^A versus σ^2 for low temperature region gives rise to 220 Ω^{-1} cm^{-1} intrinsic AHC for LaCrSb$_3$. However, if one considers the case of ultraclean limit for the present systems, the predicted AHC from skew scattering is 630 Ω^{-1} cm^{-1} (from the relation e^2/ha for $a = 6.16$ Å in LaCrSb$_3$) whereas the side-jump contributions are much smaller than e^2/ha, i.e., by an order of $\frac{\epsilon_{SO}}{E_F} \approx 10^{-1} - 10^{-3}$. Hence, even if one applies the extreme case of ultraclean limit in LaCrSb$_3$, the maximum extrinsic AHC contribution empirically is $\approx 700\ \Omega^{-1}\ cm^{-1}$. This still amounts to a minimum intrinsic AHC of $\approx 550\ \Omega^{-1}\ cm^{-1}$. It indicates that the linear intercept of σ_H^A versus σ^2 is not a good approximation for estimating intrinsic contribution of AHC in this system. Furthermore, AHE derived from BC is resonantly enhanced when $\frac{\hbar}{\tau}$ and ϵ_{SO} of materials are equivalent, i.e., $\frac{\hbar}{\tau} \cong \epsilon_{SO}$, where τ is relaxation time, $\hbar$ is the reduced Planck constant, and ϵ_{SO} is SOC energy of bands close to E_F.[30] We found that the values of $\frac{\hbar}{\tau}$ and ϵ_{SO} are 0.7 and 0.8, respectively, for the RCrSb$_3$ series of compounds, and they are best matched in the criteria of the resonantly enhanced AHE. These scenarios indicate that the measured AHC of RCrSb$_3$ can arise from a mixture of intrinsic and extrinsic origins that is hard to separate out. The low temperature longitudinal conductivity of all the three compounds is between 10^4 and $10^5\ \Omega^{-1}\ cm^{-1}$ which is still in the moderate conductivity limit, but is close to the boundary of dirty limit. Hence, the most probable cause of the extrinsic contribution can be the side-jump effect. It originates from the change in the momentum of the Gaussian wave packet when it interacts to a sufficiently smooth impurity potential in the presence of spin–orbit interaction.[3] Like the intrinsic effect, it is also independent of the scattering time and hence very difficult to differentiate.

In conclusion, we observed large values of anisotropic AHC in RCrSb$_3$ (R = La, Ce, and Nd) series of compounds. Effect of introducing f-electrons as in CeCrSb$_3$ and NdCrSb$_3$ shows enhancement in AHC. The large magnetic moment in NdCrSb$_3$ can be one of the reasons for the existence of giant AHC. We demonstrate that power law scaling for anomalous Hall conductivity follows $\sigma_H^A \propto \sigma^{1.7}$ which is valid in the intrinsic and side-jump regime for LaCrSb$_3$ and CeCrSb$_3$ while it goes beyond this scaling for NdCrSb$_3$. The positive aspects of the existence of rather dispersionless bands for observing large value of anomalous Hall conductivity have also been discussed for the first time which will provide motivation for exploring anomalous transport in flat-band magnetic systems.

Supporting Information

Supporting Information is available from the Wiley Online Library or from the author.

Acknowledgements

This work was financially supported by the European Research Council (ERC) Advanced Grant No. 742068 ("TOPMAT") and Deutsche Forschungsgemeinschaft (DFG) under SFB 1143 (Project No. 247310070).

Open access funding enabled and organized by Projekt DEAL.

Conflict of Interest

The authors declare no conflict of interest.

Data Availability Statement

The data that support the findings of this study are available from the corresponding author upon reasonable request.

Keywords

anomalous Hall effect, electrical transport, first-principles calculations, itinerant ferromagnet

Received: February 12, 2021
Revised: March 15, 2021
Published online: May 3, 2021

[1] R. Karplus, J. M. Luttinger, *Phys. Rev.* **1954**, *95*, 1154.
[2] D. Xiao, M.-C. Chang, Q. Niu, *Rev. Mod. Phys.* **2010**, *82*, 1959.
[3] N. Nagaosa, J. Sinova, S. Onoda, A. H. MacDonald, N. P. Ong, *Rev. Mod. Phys.* **2010**, *82*, 1539.
[4] M. V. Berry, *Proc. R. Soc. Lond. Ser. A* **1984**, *392*, 45.
[5] K. Sun, Z. Gu, H. Katsura, S. Das Sarma, *Phys. Rev. Lett.* **2011**, *106*, 236803.
[6] Y.-F. Wang, Z.-C. Gu, C.-D. Gong, D. N. Sheng, *Phys. Rev. Lett.* **2011**, *107*, 146803.
[7] Z. Li, J. Zhuang, L. Wang, H. Feng, Q. Gao, X. Xu, W. Hao, X. Wang, C. Zhang, K. Wu, S. X. Dou, L. Chen, Z. Hu, Y. Du, *Sci. Adv.* **2018**, *4*, eaau4511.
[8] T. Neupert, L. Santos, C. Chamon, C. Mudry, *Phys. Rev. Lett.* **2011**, *106*, 236804.
[9] E. Tang, J.-W. Mei, X.-G. Wen, *Phys. Rev. Lett.* **2011**, *106*, 236802.
[10] A. Zhao, S.-Q. Shen, *Phys. Rev. B* **2012**, *85*, 085209.
[11] J. Liu, Z. Ma, J. Gao, X. Dai, *Phys. Rev. X* **2019**, *9*, 031021.
[12] S. Peotta, P. Törmä, *Nat. Commun.* **2015**, *6*, 8944.
[13] Y. Cao, V. Fatemi, S. Fang, K. Watanabe, T. Taniguchi, E. Kaxiras, P. Jarillo-Herrero, *Nature* **2018**, *556*, 43.
[14] H. Tasaki, *Phys. Rev. Lett.* **1992**, *69*, 1608.
[15] Z. Lin, J.-H. Choi, Q. Zhang, W. Qin, S. Yi, P. Wang, L. Li, Y. Wang, H. Zhang, Z. Sun, L. Wei, S. Zhang, T. Guo, Q. Lu, J.-H. Cho, C. Zeng, Z. Zhang, *Phys. Rev. Lett.* **2018**, *121*, 096401.

[16] S. Nakatsuji, N. Kiyohara, T. Higo, *Nature* **2015**, *527*, 212.
[17] A. K. Nayak, J. E. Fischer, Y. Sun, B. Yan, J. Karel, A. C. Komarek, C. Shekhar, N. Kumar, W. Schnelle, J. Kübler, C. Felser, S. S. P. Parkin, *Sci. Adv.* **2016**, *2*, e1501870.
[18] L. Ye, M. Kang, J. Liu, F. von Cube, C. R. Wicker, T. Suzuki, C. Jozwiak, A. Bostwick, E. Rotenberg, D. C. Bell, L. Fu, R. Comin, J. G. Checkelsky, *Nature* **2018**, *555*, 638.
[19] K. Manna, L. Muechler, T.-H. Kao, R. Stinshoff, Y. Zhang, J. Gooth, N. Kumar, G. Kreiner, K. Koepernik, R. Car, J. Kübler, G. H. Fecher, C. Shekhar, Y. Sun, C. Felser, *Phys. Rev. X* **2018**, *8*, 041045.
[20] A. Sakai, Y. P. Mizuta, A. A. Nugroho, R. Sihombing, T. Koretsune, M.-T. Suzuki, N. Takemori, R. Ishii, D. Nishio-Hamane, R. Arita, P. Goswami, S. Nakatsuji, *Nat. Phys.* **2018**, *14*, 1119.
[21] E. Liu, Y. Sun, N. Kumar, L. Muechler, A. Sun, L. Jiao, S.-Y. Yang, D. Liu, A. Liang, Q. Xu, J. Kroder, V. Süß, H. Borrmann, C. Shekhar, Z. Wang, C. Xi, W. Wang, W. Schnelle, S. Wirth, Y. Chen, S. T. B. Goennenwein, C. Felser, *Nat. Phys.* **2018**, *14*, 1125.
[22] K. Kim, J. Seo, E. Lee, K. T. Ko, B. S. Kim, B. G. Jang, J. M. Ok, J. Lee, Y. J. Jo, W. Kang, J. H. Shim, C. Kim, H. W. Yeom, B. Il Min, B.-J. Yang, J. S. Kim, *Nat. Mater.* **2018**, *17*, 794.
[23] S. J. Crerar, L. Deakin, A. Mar, *Chem. Mater.* **2005**, *17*, 2780.
[24] D. D. Jackson, M. Torelli, Z. Fisk, *Phys. Rev. B* **2001**, *65*, 014421.
[25] N. P. Raju, J. E. Greedan, M. J. Ferguson, A. Mar, *Chem. Mater.* **1998**, *10*, 3630.
[26] E. Granado, H. Martinho, M. S. Sercheli, P. G. Pagliuso, D. D. Jackson, M. Torelli, J. W. Lynn, C. Rettori, Z. Fisk, S. B. Oseroff, *Phys. Rev. Lett.* **2002**, *89*, 107204.
[27] W. Jiang, D. J. P. de Sousa, J.-P. Wang, T. Low, *Phys. Rev. Lett.* **2021**, *126*, 106601.
[28] S. N. Guin, K. Manna, J. Noky, S. J. Watzman, C. Fu, N. Kumar, W. Schnelle, C. Shekhar, Y. Sun, J. Gooth, C. Felser, *NPG Asia Mater.* **2019**, *11*, 16.
[29] C. Shekhar, N. Kumar, V. Grinenko, S. Singh, R. Sarkar, H. Luetkens, S.-C. Wu, Y. Zhang, A. C. Komarek, E. Kampert, Y. Skourski, J. Wosnitza, W. Schnelle, A. McCollam, U. Zeitler, J. Kübler, B. Yan, H.-H. Klauss, S. S. P. Parkin, C. Felser, *Proc. Natl. Acad. Sci. USA* **2018**, *115*, 9140.
[30] S. Onoda, N. Sugimoto, N. Nagaosa, *Phys. Rev. Lett.* **2006**, *97*, 126602.
[31] T. Miyasato, N. Abe, T. Fujii, A. Asamitsu, S. Onoda, Y. Onose, N. Nagaosa, Y. Tokura, *Phys. Rev. Lett.* **2007**, *99*, 086602.
[32] S. Onoda, N. Sugimoto, N. Nagaosa, *Phys. Rev. B* **2008**, *77*, 165103.